

Topological spin textures in an antiferromagnetic monolayer

Felix Zahner,^{1,*} Tim Drevelow,^{2,†} Roberto Lo Conte,³
Roland Wiesendanger,¹ Stefan Heinze,^{2,4} and Kirsten von Bergmann¹

¹*Institute of Nanostructure and Solid State Physics,
University of Hamburg, Jungiusstraße 11, 20355 Hamburg, Germany*

²*Institute of Theoretical Physics and Astrophysics,
University of Kiel, Leibnizstrasse 15, 24098 Kiel, Germany*

³*Zernike Institute for Advanced Materials, University of Groningen, 9747 AG Groningen, The Netherlands.*

⁴*Kiel Nano, Surface, and Interface Science (KiNSIS), University of Kiel, Germany*

(Dated: January 1, 2026)

Topological spin structures such as magnetic skyrmions are of fundamental interest and promising for various types of applications in spintronics. Skyrmions have been predicted to emerge also in antiferromagnetic materials where they exhibit superior transport properties. They were experimentally revealed in synthetic antiferromagnets, however, still remain elusive in intrinsic antiferromagnets. Here, we demonstrate the stabilization of topological spin structures in an antiferromagnetic monolayer. Using spin-polarized scanning tunneling microscopy, we observe an antiferromagnetic spin spiral in the Mn monolayer and a collinear antiferromagnetic state in the Mn double-layer on Ta(110). Near the boundary to the double-layer half-skyrmions form in the monolayer as revealed in combination with first-principles calculations and micromagnetic simulations. Our work shows how the topological state in antiferromagnetic material systems can be controlled by the configuration within a lateral heterostructure, resulting in trivial non-coplanar states or antiferromagnetic skyrmions.

INTRODUCTION

Magnetic quasiparticles such as skyrmions and merons have been in the focus of extensive research in the last decade due to their potential application in information storage technologies [1–5]. These quasiparticles are knots in the magnetization and their local topological charge corresponds to the number of times the spins wrap the entire unit sphere. Skyrmions have integer topological charge and live in an out-of-plane ferromagnetic (FM) background, whereas merons have half-integer charge, occur in an in-plane FM background, and come in pairs often denoted as bimerons [6, 7].

For skyrmions –the most widely studied topological object– creation, annihilation, and controlled motion using lateral currents have already been demonstrated experimentally [8–11]. However, these magnetic quasiparticles show a generally undesirable transversal motion –the skyrmion Hall effect [12, 13]– which can lead to annihilation at the film boundaries. By selecting suitable boundary conditions at the film edges, skyrmion annihilation can be avoided. Engineering of film edges can also be exploited to stabilize skyrmions in zero magnetic field [14].

Recently, topological spin textures in antiferromagnets have also garnered much interest for applications in antiferromagnetic (AFM) spintronics [15, 16]. Localized windings in an AFM background [17] hold key advantages compared to their FM counterparts such as strongly reduced stray fields, faster dynamics, as well as a suppression of the skyrmion Hall effect when driven by spin-orbit torques [18, 19]. Dzyaloshinskii-Moriya interaction (DMI) induced AFM-spin spirals have been observed experimentally in single atomic layers of Mn and Cr on

W(110) [20–22], however, unlike their FM counterparts the application of an external magnetic field cannot result in localized topological states. So far, localized AFM quasiparticles have been observed mainly in layered antiferromagnets with weak interlayer coupling between two FM layers, so called synthetic antiferromagnets [23, 24]. Additionally AFM merons and antimerons have been observed at the interface between an AFM α –Fe₂O₃ thin film and a Pt overlayer with the FM sublattices still located in different layers [25]. While theoretical predictions for localized topological spin textures within the same AFM layer, where the FM sublattices are interlaced, exist [26], no experimental results have been reported so far.

Here, we exploit competing magnetic states in lateral heterostructures of AFM films to realize topological spin textures near their boundaries. Using spin-polarized scanning tunneling microscopy (SP-STM) in combination with density functional theory (DFT) calculations and micromagnetic simulations, we reveal the spin texture of the Mn monolayer (ML) and Mn double-layer (DL) on the Ta(110) surface. The Mn DL hosts a collinear AFM state with an easy out-of-plane magnetization axis. At the boundary to the Mn ML –exhibiting an AFM spin spiral state– this leads to frustration and results in the formation of localized non-coplanar spin textures within the Mn ML. These intriguing objects are identified as half-skyrmions with a topological charge of $|\frac{1}{2}|$ on each sublattice. We further demonstrate that for a Mn ML region sandwiched between two regions of the Mn DL, the half-skyrmions on each side can either be of opposite topology, leading to a globally trivial magnetic system, or they combine to form topological AFM skyrmions.

EXPERIMENTAL RESULTS

Our samples were prepared in ultra-high vacuum and then transferred *in-situ* to a low-temperature STM. The Ta(110) single crystal was flashed to $T > 2300$ K and subsequently Mn was deposited onto the warm surface at a rate of about 0.2 atomic layers per minute from an effusion cell. The Mn ML almost fully wets the substrate, with the Mn DL growing from the step edges. As already found in our previous work both layers grow pseudomorphically [27].

Using a spin-polarized tip we observe a stripe pattern on the ML in constant-current measurements, both in the height and the current channel (see methods for more details). The stripes along [001] in the SP-STM image of Fig. 1a appear with a period of approx. 466 pm, originating from the AFM order [27, 28]. The magnetic stripe pattern in the ML vanishes periodically indicating the presence of a spin spiral with a propagation in the [001] direction (see sketch in Fig. 1b). From field-dependent measurements with soft-magnetic Fe/W-tips we can confirm that both out-of-plane (OOP) and in-plane (IP) regions are present in the Mn ML, see Supplementary Fig. S1. Due to the high spin-orbit coupling of Ta a significant contribution from interface-DMI can be expected, and consequently we conclude that the spin rotation is of cycloidal nature as depicted in Fig. 1b, similar to previous interface-DMI induced AFM spin spirals in a Cr and Mn ML on W(110) [20–22].

We have extracted and averaged multiple line profiles along the [001] direction, see Fig. 1c. A fit with a sinusoidal function reveals that a spin rotation of 360° is completed every 18.5 nm. Adjacent atomic rows have an inverted magnetization, meaning that the spins are perfectly OOP every 9.25 nm. The same holds true for IP regions. The deviation from the sinusoidal fit is quite small indicating a nearly homogeneous undistorted spin spiral.

An overview constant-current image of a sample with ≈ 1.25 AL is shown in Fig. 2a. A current map of the sample area indicated by the black rectangle is displayed in Fig. 2b, showing a stripe pattern also on the DL. Note that on the DL there is no additional modulation, demonstrating that this is a collinear AFM [27, 28]. We find that the DL has some effect on the magnetic state in the adjacent ML as we do not observe any modulation in the ML region next to the DL area, see Fig. 2b, whereas in regions further away the spin spiral persists (see upper part of the image). We conclude that the rotation of the spins is suppressed near the DL. After a modification of the tip apex, the current map does not show any magnetic contrast on the DL, see Fig. 2c. Based on field-dependent measurements with a soft-magnetic Fe/W-tip that show the AFM state is aligned in the OOP direction both for the DL and the ML next to it, see Fig. S1,

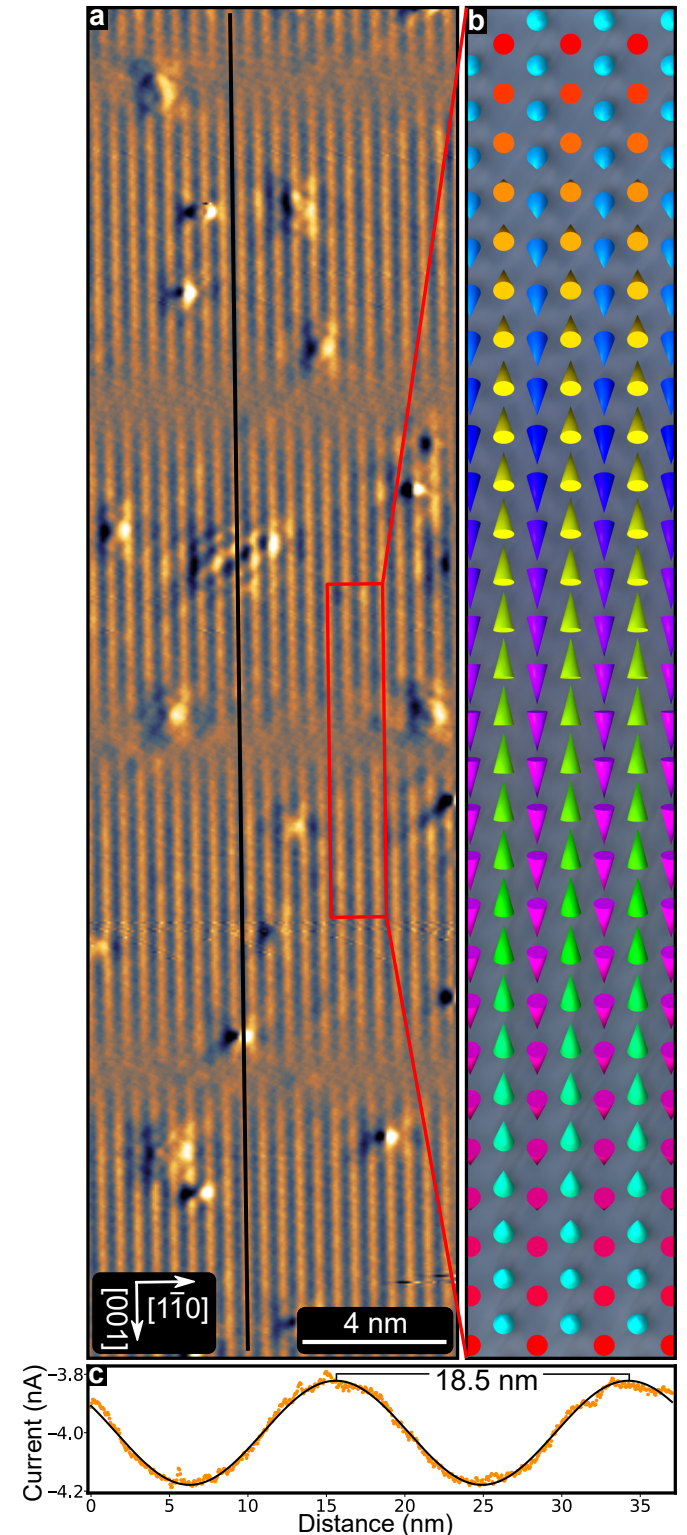


Figure 1. AFM spin spiral ground state of the Mn ML on Ta(110). **a**, SP-STM current map of the AFM spin spiral in the Mn ML. $U = -15$ mV, $I = 4$ nA. **b**, Sketch of an AFM cycloidal spin spiral. Each cone represents the position and magnetic moment of an atom, with the color encoding the magnetization in the [001]-[110]-plane. **c**, Line profile of the AFM spin spiral along the propagation direction as marked by the black line in **a**. 18 line-profiles from **a** were averaged for this plot.

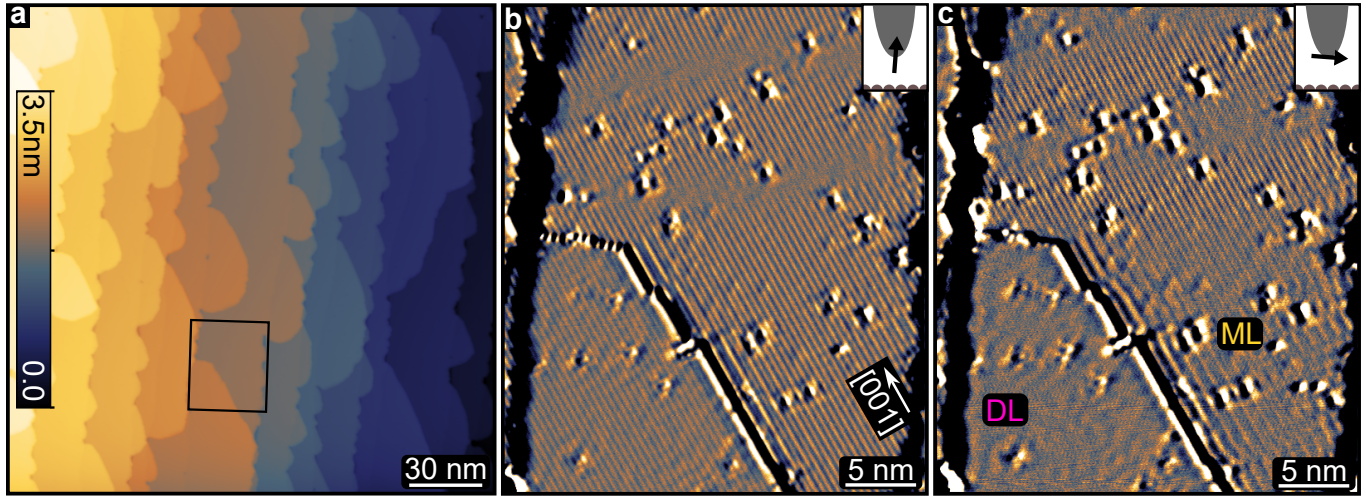


Figure 2. Magnetic state of the Mn ML and Mn DL on Ta(110). **a**, Constant-current STM topography image of 1.25 atomic layers of Mn on Ta(110). $U = +600$ mV, $I = 500$ pA. **b,c**, Constant-current SP-STM current images of a Mn ML terrace with a region of Mn DL grown on top (bottom left), measured with two different tip magnetization directions. $U = -15$ mV, **b**: $I = 2$ nA, **c**: $I = 5$ nA.

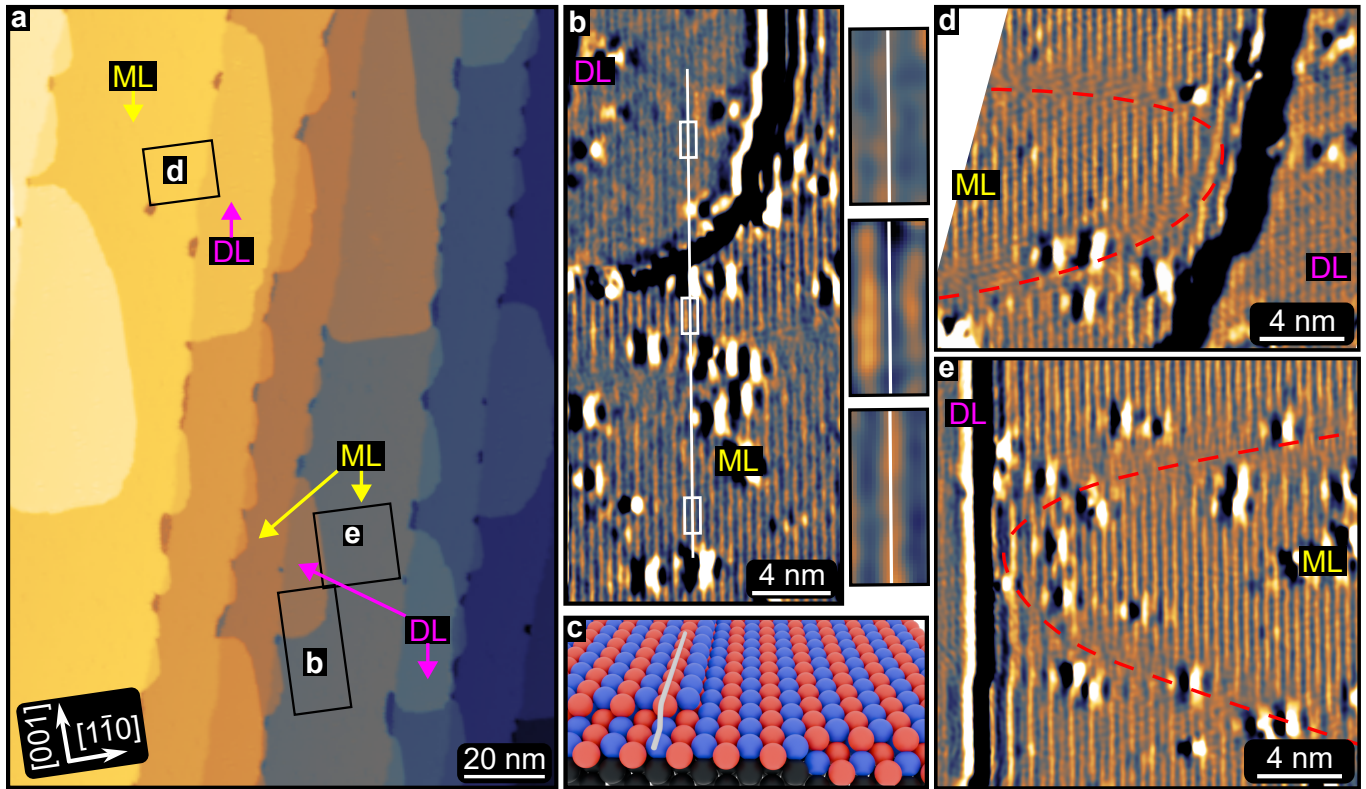


Figure 3. Half-loop formation at the DL/ML boundary. **a**, Constant-current STM image of a sample with 1.25 atomic layers of Mn on Ta(110). $U = +200$ mV, $I = 300$ pA. **b**, SP-STM current image of a region of DL (top) growing on the ML (bottom). Scan area marked in **a**. Insets on the right show enlarged views of the regions indicated by white rectangles. $U = -15$ mV, $I = 1$ nA. **c**, Sketch of Mn atoms (red and blue) on Ta (black). Red and blue color encode the spin direction of the Mn atoms. The white line follows a path similar to the line in **b**. Some Mn atoms in the DL were removed in the front. **d**, SP-STM current image of a ML region (left) bordering to DL across a buried Ta step edge (right). Scan region marked in **a**. $U = -15$ mV, $I = 1$ nA. **e**, SP-STM current image of a region of ML bordering a DL island growing on top (left side). Scan region marked in **a**. $U = -15$ mV, $I = 3$ nA. For **b,d,e** high frequency noise was removed. Raw data can be seen in the Supplementary Information.

we can conclude the tip magnetization has changed from OOP (Fig. 2b) to IP (Fig. 2c). Consequently the regions of magnetic stripe pattern and vanishing magnetic signal on the ML are interchanged, see Fig. 2b-c. Near [001] boundaries we observe standing electron waves on the ML with a period of approx. 0.9 nm, see Fig. 2c. When these standing electron waves coexist with the magnetic stripe pattern, which has roughly half the period, a beating pattern is observed, see Fig. 2b.

To investigate the interplay of the magnetism in the DL and the adjacent ML regions, we characterize the phase relation between their AFM states. Fig. 3a shows a stepped surface with multiple DL islands attached to the step edges and a nearly closed ML. A current map of a region with DL and ML is shown in Fig. 3b. The insets to the right show zoomed-in views of the areas marked by the white rectangles and can be used to identify the phase relation. The stripe patterns in the DL and the closest ML region are out-of-phase and we conclude that the two layers are aligned antiferromagnetically, see left side of the sketch in Fig. 3c, analogously to what was observed for Mn MLs and DLs on Nb(110) [29] and expected for AFM interlayer coupling.

On a stepped surface the ML regions can have a boundary to the DL not only when there is an additional layer on top, as in Fig. 3b, but also when the ML extends across a buried Ta step edge and transforms into the upper layer of a DL region, see right side of the sketch in Fig. 3c. While for small ML regions the spin spiral can be fully suppressed, larger ML regions develop the AFM spin spiral ground state. However, in the vicinity to a DL region we still observe the presence of an imposed collinear region, which leads to half-loop formation of the in-plane spin spiral regions, see Fig. 3d and 3e for the two different DL-ML boundaries. Even though these half loops are not easy to resolve due to defects and standing-electron waves, we understand that they cut off the unfavorable OOP-AFM region near the DL-ML boundary.

The question arises, what happens when a ML region is connected to a DL on both sides. We expect that during the cooling of the sample from the preparation temperature down to 4.2 K the magnetic order in the DL regions is established first, as we should expect a higher Néel temperature for the thicker film. This AFM state can arise in two different phase-shifted states with respect to the underlying atomic lattice, meaning that the AFM state of neighboring DL islands can be either in-phase or out-of-phase.

In the case of an out-of-phase configuration the two DL islands favour opposite OOP regions of the adjacent ML, and a magnetic boundary must form in the ML. Figure 4a shows such a case and the green dots mark favorable DL/ML configurations. At frustrated DL/ML regions, indicated by red dots, a half-loop must form. Instead of forming a straight domain wall, the phase shift between the two DL regions leads to a spin spiral state with half-

loops on both sides, with the in-plane spins of the ML forming one continuous serpentine line (indicated in red). However, even in the center of the ML of Fig. 4a the spin spiral is not fully developed, as evident from the tilting of the IP regions away from the [110] direction.

When the magnetic state of two neighboring DL regions is in-phase the situation is different. For very slim terraces, as the one displayed in Fig. 4b, the spin spiral ground state can develop in the middle of the ML region, see line profile shown in Fig. 4c, which demonstrates that the phase of the stripe pattern alternates in the center of the ML region, whereas it is in-phase all along the DL/ML boundary, see Fig. 4d. We find that the half-loops, that form near the two boundaries to the DL regions, form pairs, which leads to elliptical loops of in-plane spins in the otherwise out-of-plane magnetized ML.

FIRST-PRINCIPLES CALCULATIONS

To understand the experimental observations we have performed first-principles calculations via DFT for the Mn ML and DL on Ta(110) (see methods for computational details). For the structurally relaxed Mn ML on Ta(110) (see Supplementary Table I), we have calculated the energy dispersion of spin spirals. Thereby, we scan a large part of the magnetic phase space since spin spirals are the general solution of the Heisenberg model on a periodic lattice. A spin spiral propagates along the wave vector \mathbf{q} and the magnetic moment at lattice site \mathbf{r}_i is given by $\mathbf{M}_i = M(\cos(\mathbf{r}_i \cdot \mathbf{q}), \sin(\mathbf{r}_i \cdot \mathbf{q}), 0)$, where M denotes its magnitude. Note that without spin-orbit coupling (SOC), the plane of rotation can be chosen arbitrarily. The energy minimum of the spin spiral dispersion neglecting SOC (Fig. 5a) is obtained for the AFM state occurring at the \bar{N} -point, while the FM state ($\bar{\Gamma}$ point) is energetically highest. Interestingly, a similarly high energy is found at the \bar{F} -point corresponding to another AFM state with ferromagnetic rows along [111]. The high energy at the $\bar{\Gamma}$ and the \bar{F} point can be attributed to a strong AFM nearest and FM next-nearest neighbor coupling, respectively.

To explore the effect of DMI on the magnetic ground state, we focus now on the energy dispersion in the vicinity of the \bar{N} -point along both high symmetry directions (Fig. 5b,c). If SOC is neglected, left- and right-rotating spin spirals are energetically degenerate (blue symbols and curves) and the AFM state at $\Delta q = 0$, i.e. the \bar{N} point, is the energy minimum. Upon including SOC in the DFT calculations the DMI arises (see methods) and the energy minima shift from the AFM state towards spin spiral energy minima with periods of

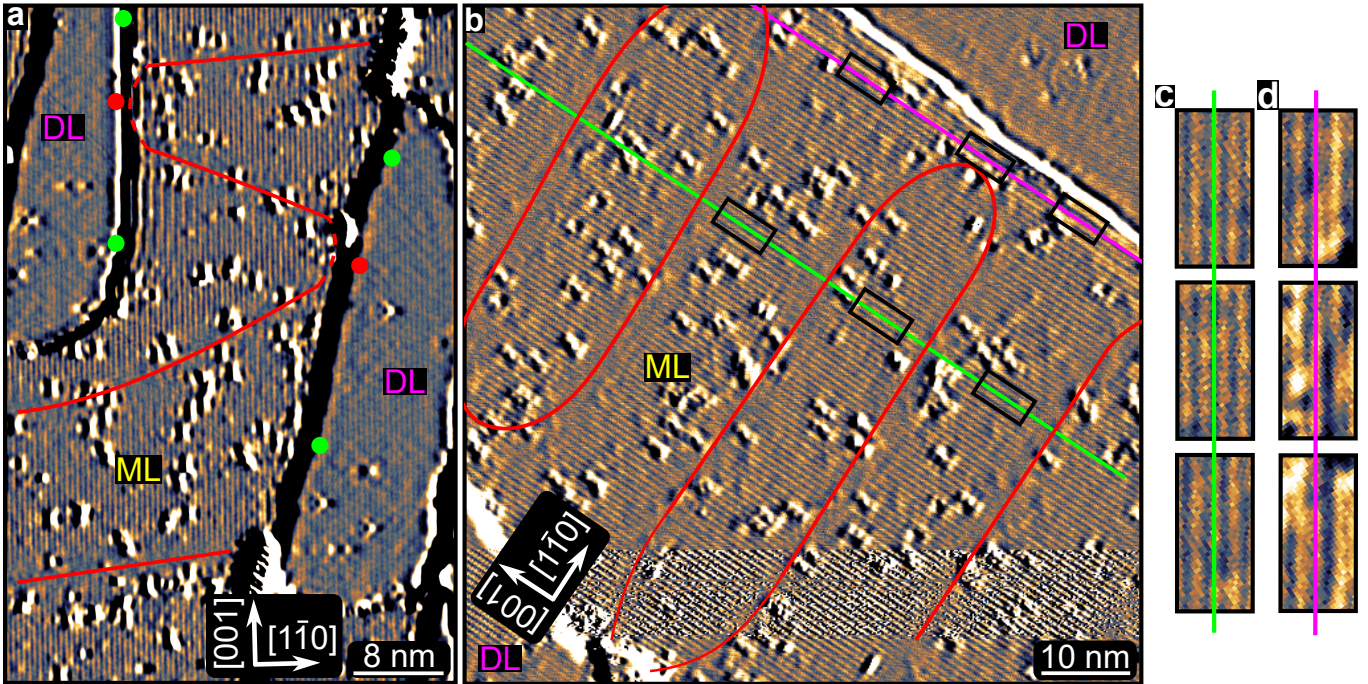


Figure 4. Effect of the phase relation between DL regions on the magnetic state in the ML. **a**, SP-STM current image of a sample with 1.25 atomic layers of Mn. The red lines indicate areas with mainly IP spin alignment. The green/red circle indicate favorable/unfavorable regions at the DL/ML interface. $U = -15$ mV, $I = 1$ nA. The high frequency noise was removed (see Supplementary Information for raw data). **b**, SP-STM current image of a large ML area with regions of DL at top right and bottom left. The red lines indicate the regions with mainly IP spin alignment. $U = -10$ mV, $I = 1$ nA. **c,d**, Enlarged views of the regions indicated by the black rectangles on the green/pink line in **b**.

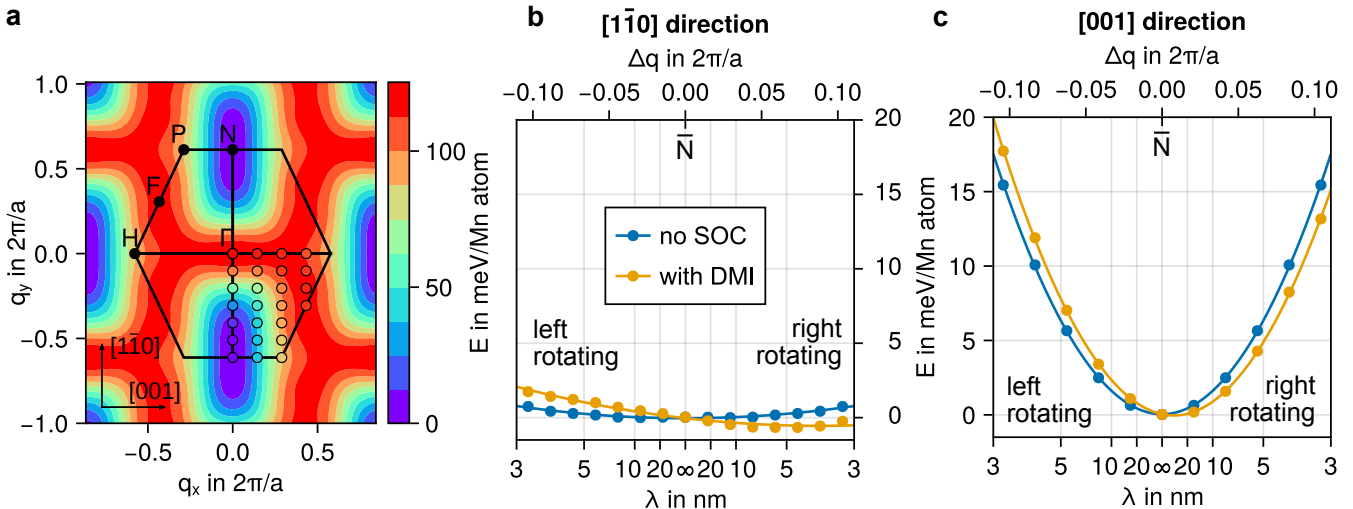


Figure 5. DFT energy dispersions of spin spirals in a Mn ML on Ta(110). **a**, Energy dispersion of spin spirals in the two-dimensional Brillouin zone in the Mn monolayer on Ta(110). Color-coded circles represent DFT results, while the coloring of the background represents an interpolation. **b** and **c** show zoomed-in regions along the $\bar{N}\bar{F}$ and $\bar{N}\bar{P}$ paths around the \bar{N} -point, respectively. The energy is displayed over the period of the spiral distortion λ with respect to the \bar{N} -point. The DFT data, represented as circles, is fitted with parabolas representing the fit with a micromagnetic model. Data without SOC is blue, data with SOC in first order perturbation theory, which can be attributed to DMI, is shown in yellow.

System	[1̄10]	[001]	[110]
Mn ML/Ta(110)	0.00	-1.71	-2.23
Mn DL/Ta(110)	0.00	-0.35	-0.96

Table I. Magnetocrystalline anisotropy values determined by DFT. The values of the MAE are given for a Mn monolayer and a Mn double-layer on the Ta(110) surface calculated in the AFM state via DFT for the three main crystallographic directions, with the hardest [1̄10] direction as a reference value. The energies are given in meV per Mn atom.

$\lambda_{[1̄10]} = 3.8$ nm and $\lambda_{[001]} = 43.3$ nm for the two high-symmetry directions. In the vicinity of the \bar{N} -point, the DMI prefers a rotation in the plane spanned by the [110] (out-of-plane) direction and the relative spin spiral vector $\Delta\mathbf{q}$, i.e. cycloidal spin spirals emerge. In this film system right-rotating spin spirals are favored by the DMI for both high-symmetry directions. Note that both energy minima are extremely shallow with energies of only -1.54 meV/Mn atom (Fig. 5b) and -0.25 meV/Mn atom (Fig. 5c) with respect to the AFM state for spin spirals along the [1̄10] and the [001] direction, respectively.

As the energy difference between the spin spirals due to exchange and DMI is very small, the contribution of the magnetocrystalline anisotropy energy (MAE) can become important. Surprisingly, the MAE obtained via DFT for the Mn ML on Ta(110) (see methods) is larger than the DMI energy contribution (see Tab. I). The MAE values follow the general trend $E_{[110]} < E_{[001]} \ll E_{[1̄10]}$, i.e. the out-of-plane direction is the easy magnetization axis and the [1̄10] in-plane direction is extremely unfavorable. The hard [1̄10]-axis lowers the energy of the spin spiral along [001], which is the one observed experimentally. However, the total DFT energy of the spin spiral along [1̄10] is still slightly lower by 0.9 meV.

For the Mn DL on Ta(110) we obtain an AFM ground state as it is the energetic minimum in spin spiral calculations (Supplementary Figure S4). In the AFM state the two layers couple antiferromagnetically. We find that the magnetic moment in the bottom Mn layer is quite small with about $1.01\ \mu_B$, whereas it is $2.73\ \mu_B$ in the top Mn layer. Configurations with a FM coupling cannot be stabilized in our DFT calculations, as the bottom Mn atoms flip their moments into an AFM alignment during DFT self-consistency cycles. This indicates, together with its small magnitude, that the Mn moment of the bottom layer is not intrinsic and only induced by the top layer, which dictates the direction of its magnetic moments. A similar effect has been reported for a Mn DL on W(001) [30]. Regarding the MAE (see Tab. I), we find the trend: $E_{[110]} \ll E_{[001]} < E_{[1̄10]}$. Because the out-of-plane direction is strongly favored over the IP direction while the DMI in the DL is very weak (Supplementary Figure S4c), a spin spiral formation is suppressed and the magnetic ground state of the DL is a collinear out-of-plane AFM state consistent with the experimental ob-

servations.

MICROMAGNETIC SIMULATIONS

The large spin spiral periods and flat energy landscape found via DFT near the \bar{N} -point (AFM state) of the energy dispersion suggest that any spin structure in the Mn ML on Ta(110) is locally close to the AFM state on the atomic scale (~ 0.3 nm), with distortions and rotations on a much larger scale (~ 10 nm). A treatment of such spin spirals is not feasible in an atomistic spin simulation because of the large number of interacting atomic moments. However, the difference in length scales, allows us to investigate this system in the micromagnetic model. In order to apply micromagnetic simulations to this AFM system we simulate one of its FM sublattices with the same energy dispersion around the $\bar{\Gamma}$ point (FM state) as the Mn ML exhibits around the \bar{N} -point (AFM state). Therefore, both systems produce the same energy density dispersions $E(\Delta q)/\Omega_{UC} = \frac{1}{2}A\Delta q^2 + D\Delta q$ per unit cell area Ω_{UC} along both high symmetry directions which can be parametrized by the DFT total energy data from Fig. 5b and 5c, considering states near the \bar{N} -point ($|\Delta\mathbf{q}| \leq 0.11 \cdot 2\pi/a$). The obtained parameters of the micromagnetic model, i.e. the exchange stiffness A and the DMI constant D , are given in Supplementary Table II.

The experiments have shown that magnetic frustration can occur at boundaries between the cycloidal spin spiral, which occurs in the Mn ML, and the collinear AFM state in the Mn DL on Ta(110). To investigate this boundary, micromagnetic simulations of the (locally) FM sublattices were performed within the following set-up (see Methods for details): A ML stripe extends along the [001] direction with periodic boundary conditions. This Mn ML stripe is sandwiched between two DL regions. In the DL regions, there is an easy axis MAE along the [110] (out-of-plane) direction, which stabilizes a rigid FM state, while in the ML, the MAE exhibits a hard axis along [1̄10]. Note, that due to the restriction of only using uniaxial anisotropy, the MAE difference between the [110] and the [001] direction in the ML vanishes, which leads to a homogeneous spin spiral with a period of 43.3 nm.

The results of a micromagnetic simulation can be seen in Fig. 6a. While a wide ML stripe is used in the simulation, we first focus on the boundary between the two different regions where half-loops were found in the experiments. The DL regions are aligned completely along the out-of-plane direction due to the MAE (white for up- and black for downwards magnetization). In the middle of the ML stripe, a cycloidal spin spiral emerges as the ground state, stabilized by the DMI with its direction determined by the hard axis due to the MAE. Towards the DL the regions of opposite out-of-plane magnetization (black) gets

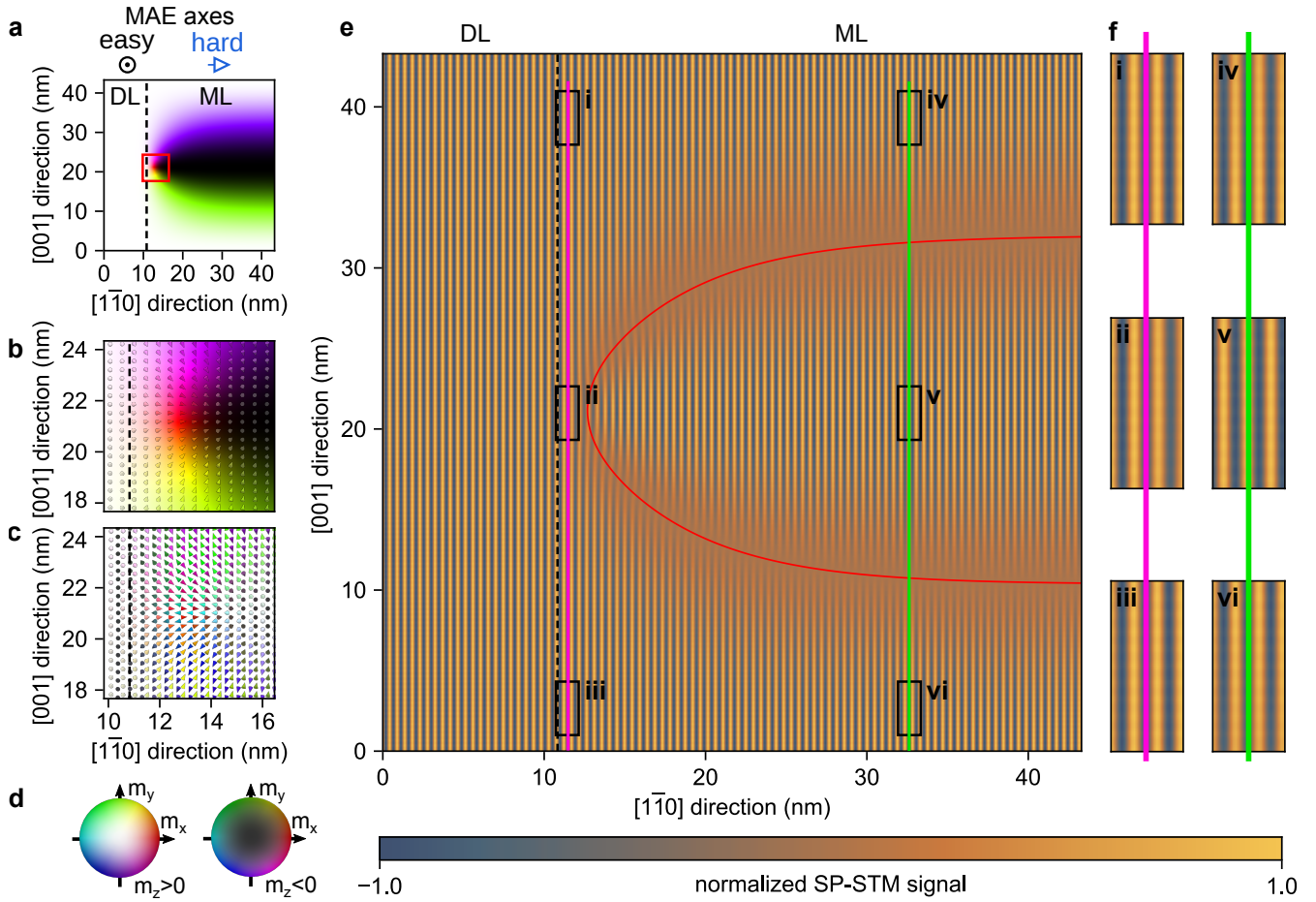


Figure 6. Antiferromagnetic half-sklyrmion spin textures at a Mn ML/DL interface on Ta(110). **a** and **b** show the color-coded magnetization densities $\mathbf{m}(\mathbf{r})$ obtained from micromagnetic simulations of a FM system equivalent to the AFM Mn film; the area of **b** is indicated by the red square in **a**. **d** shows the color code used for the magnetization. In **b** and **c**, color-coded cones represent the magnetization direction. The axes of the magnetocrystalline anisotropy are shown above **a**. While the DL regions are oriented out-of plane (white), the ML exhibits a homogeneous spin spiral at large distance to the DL. In the zoomed-in region in **b**, a closing of the downwards magnetized areas (black) becomes visible that looks similar to the deformed half of a magnetic skyrmion. **b** and **c** illustrate the transition from a micromagnetic model to atomistic magnetic moments. In **b**, the interpolated, continuous magnetization density $\mathbf{m}(\mathbf{r})$ (left) is probed on the atomic positions \mathbf{r}_i (dots). In **c**, every other row is flipped to obtain the antiferromagnet. **e**, SP-STM simulation for the magnetization density shown in **a**, projected back onto the antiferromagnetic lattice of Mn atoms on a Ta(110) surface as illustrated in **c**. An out-of-plane direction of the tip magnetization has been assumed in the simulations. The red lines indicate local in-plane magnetization. **f**, Zoomed-in areas from **e**, similar to the experimental data from Fig. 4c and 4d.

thinner and are eventually cut off. (see Fig. 6a,b). At these points, the magnetization $\mathbf{m}(\mathbf{r})$ remains continuous, and points along the hard $[1\bar{1}0]$ axis, with a direction determined by DMI. Especially, the zoom into the magnetization shown in Fig. 6b looks similar to one half of a magnetic skyrmion. In order to obtain the spin structure in the Mn ML, the micromagnetic representation as a magnetization density $\mathbf{m}(\mathbf{r})$ has to be transformed back to a set of atomistic magnetic moments \mathbf{m}_i at the lattice sites \mathbf{r}_i . This procedure is illustrated in Fig. 6c. The magnetization $\mathbf{m}(\mathbf{r}_i)$ at the position \mathbf{r}_i is interpolated, then the magnetic moment of every other row is flipped to locally produce the AFM version of this state.

For a direct comparison of the resulting spin structure at the Mn ML/DL interface (Figs. 6c) with the experiments, we have performed SP-STM simulations (see methods for computational details). The simulated SP-STM image of this AFM topological spin texture assuming a tip magnetization normal to the surface is shown in Fig. 6e and can be directly compared to the experimental images (cf. Fig. 4). The stripe pattern of the AFM state is visible in the DL (left part of Fig. 6e). On the far right side of the SP-STM image, i.e. in the ML, we obtain the characteristic contrast of the spin spiral along the $[001]$ direction with AFM order (cf. Fig. 1). The vanishing SP-STM contrast for an in-plane direction of

the local magnetization ($m_z(\mathbf{r}) = 0$) is also apparent and marked by red lines. The obtained profile near the ML/DL boundary (boxes (i) to (iii) in Figs. 6e,f, magenta line) is similar to that from the SP-STM measurements shown in Fig. 4d. The SP-STM simulation also exhibits a reversal of contrast inside the loops in Fig. 6e,f (boxes (iv) to (vi), green line), which is consistent with the experiments (cf. Fig. 4c). Based on the good agreement between the simulated and measured SP-STM images we conclude that the experimentally observed half-loops at the ML/DL boundary are AFM half-skyrmions.

In the micromagnetic model the out-of-phase and in-phase AFM DL regions, that sandwich a ML region between them, are equivalent to antiparallel and parallel aligned FM DL regions, see Fig. 7a and d, respectively. In these overview images of the micromagnetic simulations, which show the full width of the sandwiches, areas of upward and downward OOP magnetization are white and black, respectively. For the case of antiparallel alignment of the FM DL (corresponding to the out-of-phase AFM DL, see Fig. 4a), we find a winding in-plane region that separates oppositely magnetized OOP regions (Fig. 7a). To determine the topological properties of the system, its topological charge density

$$\rho(\mathbf{r}) = \frac{1}{4\pi} \mathbf{m}(\mathbf{r}) \cdot \left(\frac{\partial \mathbf{m}(\mathbf{r})}{\partial x} \times \frac{\partial \mathbf{m}(\mathbf{r})}{\partial y} \right) \quad (1)$$

is computed, which can be seen in Fig. 7b. The topological charge is concentrated at the half-loops near the boundaries to the DL, with topological charge of $Q_\Omega = \int_\Omega \rho(\mathbf{r}) d\mathbf{r} = -\frac{1}{2}$ on the left boundary, and $+\frac{1}{2}$ on the right side (Fig. 7c), as expected for half-skyrmions. However, for this configuration this results in a vanishing total charge $Q = \int \rho(\mathbf{r}) d\mathbf{r} = 0$. In contrast, for the case of parallel aligned FM DL regions, Fig. 7d (corresponding to in-phase AFM DL regions, see Fig. 4b), the half-loops on both sides hold the same topological charge of $-\frac{1}{2}$ (see Fig. 7e,f). This adds up to a total topological charge of $Q = -1$, demonstrating that each closed loop is equivalent to one skyrmion in the micromagnetic simulations, corresponding to an AFM skyrmion in the experiments.

DISCUSSION

The magnetic properties of the Mn ML and DL on Ta(110) are dominated by AFM exchange interactions. However, while the DL is a collinear out-of-plane antiferromagnet, the magnetism of the ML is more complex. Due to substantial DMI the system forms a non-collinear spin spiral ground state with local AFM order. Our DFT calculations show that the propagation direction of the spin spiral, with an experimentally determined period of about 20 nm, is governed by a hard axis MAE along [1 $\bar{1}$ 0], resulting in a cycloidal modulation of the spin texture along [001].

In the vicinity of the Mn DL, the Mn ML is also found to be in a collinear AFM state. This local suppression of the spin spiral order in the Mn ML originates from the strong AFM coupling to the collinear out-of-plane spins in the Mn DL, inducing local out-of-plane order in the Mn ML. Consequently, the in-plane regions of the spin spiral are expelled from the boundary region, leading to a connection of adjacent in-plane segments and the formation of half-loop structures. Our micromagnetic simulations based on DFT parameters reveal that these half-loop structures resemble AFM half-skyrmions with a topological charge of $|\frac{1}{2}|$. At a ML/DL boundary in the [001]-direction this results in an array of AFM half-skyrmions with a spacing of the spin spiral period, i.e. about 20 nm.

When another DL is attached at the other side of the ML film, the half-loops connect in two different ways depending on the phase relation between the two DL AFMs. If the two DL AFMs are out-of-phase, then the half-loops connect to form one serpentine in-plane domain wall, which retains the spiral-like structure in the middle of the ML. In this case, the half-loops on either side possess opposite topological charges which cancel. If the two DL AFMs are in-phase, then pairs of half-loops connect to form elongated AFM skyrmions. While the simulations suggest that both of these states –the topologically trivial domain-wall-like structure and the topological AFM skyrmions– exist in the ML even for small distances between adjacent DL regions (Supplementary Figure S3), experimentally we almost always find a complete suppression of the spin spiral for ML areas with a width < 20 nm. This implies that DL regions spaced less than 20 nm apart are typically in-phase, suggesting that the DL regions are not fully independent at these distances.

The mechanism of half-loop formation essentially relies on the presence of two types of magnetic layers: one with a strong collinear order, the other with a unidirectional spin spiral ground state. The former serves as a boundary that suppresses the non-collinear order of the latter in its vicinity. The formation of AFM skyrmions in the central region can be expected when the two boundaries to the adjacent collinear regions are parallel to the propagation direction of the spin spiral. A low symmetry with a two-fold rotation axis is required to define the propagation direction of the spin spiral and a broken inversion symmetry is necessary to allow the DMI to dictate a unique rotational sense of the spin texture. The former can be achieved by a low-symmetry crystal surface, as the bcc(110) surface used here, or for instance by strain engineering, and the latter is always present at surfaces or interfaces. In case of an in-plane AFM system that confines the AFM spin spiral on both sides one can obtain chains of AFM meron- and antimeron-like states near the boundary. However, because the rotational sense in the [1 $\bar{1}$ 0] direction is not dictated by the DMI for this symmetry, the type of the localized

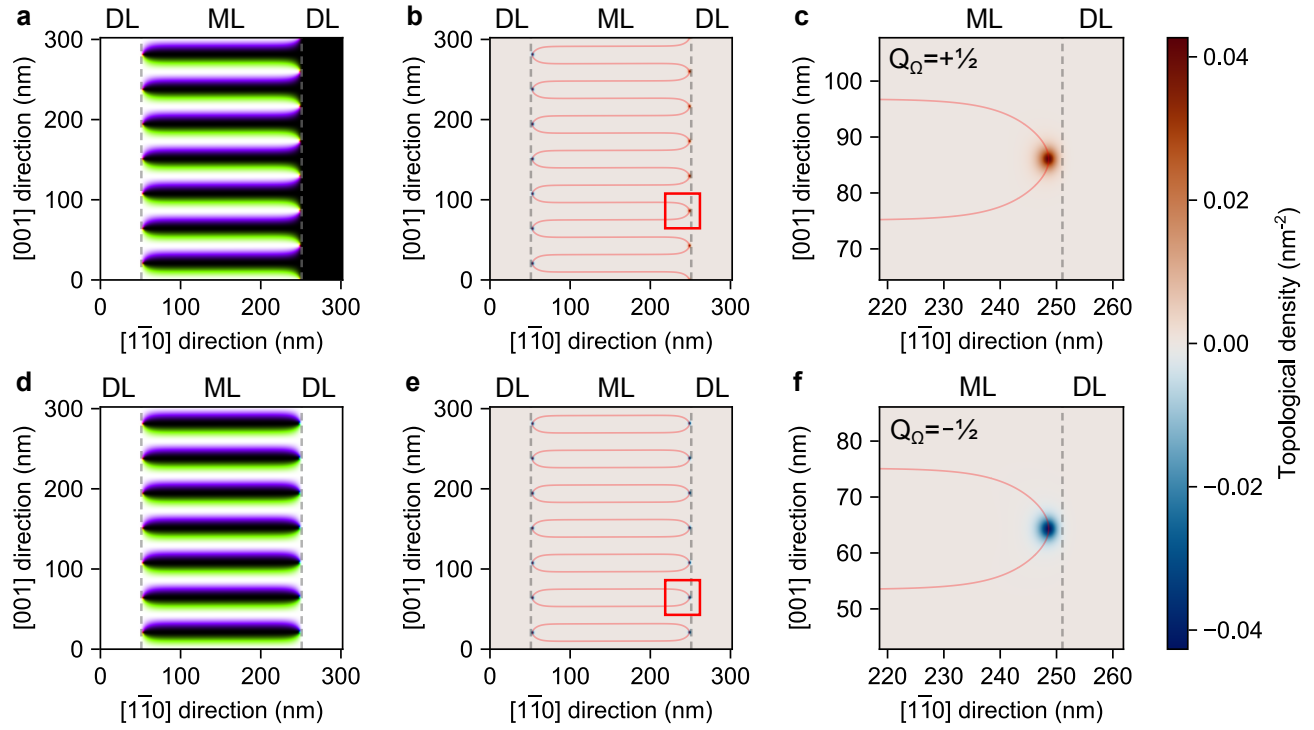


Figure 7. Topological properties of spin structures in DL-ML-DL heterostructures. **a**, Minimized magnetization density of a Mn ML sandwiched between two anti-parallel aligned DLs. **b**, Topological density in the same area as **a**. For orientation, lines of in-plane magnetization are shown in faint red. **c** is a zoom into the red area in **b**. Areas of topological charge are localized at the very end of the in-plane magnetization. They carry a topological charge about $+\frac{1}{2}$ on the border to the downwards magnetization on the right, and $+\frac{1}{2}$ on the border to the upwards magnetization on the left. **d-f** show the same plots as **a-c**, but for identical magnetic domains in the two DLs. It illustrates that a flip of the domain magnetization results in a change of sign in the topological charge as well. For this alignment of domains, both sides of a closed loop carry half the charge of a magnetic skyrmion.

objects is arbitrary. Such an engineering of the lateral boundaries of an AFM spin spiral material is a means to generate AFM skyrmions, which are otherwise difficult to stabilize. As demonstrated by our work, the relative configuration of the two boundaries allows for the formation of either topologically trivial serpentine-like domain walls or a chain of AFM skyrmions.

METHODS

Sample preparation and STM experiments. The sample preparation and measurements were done in a multi-chamber UHV system at typical operating pressures of $< 2 \cdot 10^{-10}$ mbar. The clean Ta(110) was prepared by flash annealing to > 2300 K on an electron-beam heating stage to remove the oxygen from the surface, see also [31]. Mn was then deposited shortly after, while the sample was still at elevated temperatures of $100^\circ - 200^\circ$ C. The Mn was evaporated with a Knudsen cell held at 690° C resulting in a deposition rate of approx. 0.2 atomic layers per minute. The sample was then cooled down to 4.2 K inside the STM. The measure-

ments were performed at a temperature of 4.2 K using a Cr-bulk tip. For almost all SP-STM constant-current measurements the magnetism-related signal was found to be stronger in the current-channel as compared to the topographic channel. Also an adjustment of scan speed and feedback loop did not significantly shift the magnetic signal to the topographic channel, therefore the measurement parameters were optimized to show the magnetic signal in the current channel.

First-principles calculations. To determine the lattice constants and geometry of the film system DFT calculations were performed using the VASP code [32, 33], in the generalized gradient approximation (GGA) using the exchange-correlation potential by Perdew and Wang [34]. The Ta crystal surface was modeled by a symmetric slab containing 13 atomic Ta layers with one/two atomic layers of Mn on each side. A 25×25 k -point grid in a two-atomic unit cell and an energy cutoff for the plane-waves of 400 eV was used. The theoretically determined Ta lattice constant with a GGA exchange correlation potential of 0.3321 nm was used for all calculations. The interlayer distances and magnetic moments obtained from the structural relaxations of the films can be found in

Supplementary Table I.

DFT calculations of collinear and non-collinear spin states with and without spin-orbit coupling (SOC) were carried out with the FLEUR code [35] (version MaX 6.0) in the local density approximation (LDA) of the exchange-correlation potential using the parametrization of Vosko, Wilk, and Nusair [36]. For the Mn ML and DL on Ta(110) we used asymmetric films consisting of 12 layers of Ta in (110) orientation with one and two Mn layers on only one side of the film, respectively. The interlayer distances were chosen according to the values from the structural relaxations. The energy dispersions of spin spirals have been calculated within the FLEUR code based on the generalized Bloch theorem [37]. The DMI contribution to the energy dispersions has been obtained including SOC in first-order perturbation theory [38]. A basis function cutoff of $k_{\max} = 4.1 \text{ a.u.}^{-1}$ and a 96×96 k -point grid were used for spin spiral calculations in the chemical unit cell. MAE calculations were carried out in the two-atomic unit cell with a basis function cutoff of $k_{\max} = 4.3 \text{ a.u.}^{-1}$ and a 40×57 k -point mesh, with the inclusion of SOC in self-consistent calculations [39] for the AFM state.

Micromagnetic simulations. Micromagnetic calculations were carried out using the **umax³** code [40, 41]. The film was modeled by $512 \times 512 \times 1$ grid, consisting of $0.59 \text{ nm} \times 0.59 \text{ nm} \times 0.5 \text{ nm}$ cells. The size of the system was chosen to be 7 times the wavelength of the cycloidal spin spiral in the ML. Each micromagnetic cell spans about 3 chemical unit cells, calculations with a coarser $256 \times 256 \times 1$ grid yielded results in quantitative agreement. Magnetic structures were minimized by solving the Landau-Lifschitz-Gilbert equation without the precession term. The considered micromagnetic energy

$$E = \int_{\Omega} A (\nabla \cdot \mathbf{m}(\mathbf{r}))^2 - K(\mathbf{r}) (\mathbf{m}(\mathbf{r}) \cdot \mathbf{e}_u(\mathbf{r}))^2 + D (\nabla \cdot \mathbf{m}(\mathbf{r}) - \mathbf{m}(\mathbf{r}) \cdot \nabla) m_z(\mathbf{r}) d\mathbf{r}, \quad (2)$$

in the simulation area Ω depends on the exchange stiffness A , MAE strength $K(\mathbf{r})$, MAE axis $\mathbf{e}_u(\mathbf{r})$ and DMI strength D . For the entire system, the micromagnetic constants $A_{[001]} = 8.19 \cdot 10^{-21} \text{ J}$ and $D_{[001]} = 2.38 \cdot 10^{-12} \text{ J/m}$ obtained for a spin spiral propagation along the [001] direction in the ML were chosen. This was done because the exact modeling of the DL does not play a crucial role, since its FM ground state in the micromagnetic simulations is robust over a wide range of parameters, including $A_{[001]}$ and $D_{[001]}$ from the monolayer. In the ML, the MAE has a hard axis along $\mathbf{e}_{u,ML}(\mathbf{r}) = [1\bar{1}0]$, and a strength of $K_{ML} = 4.58 \text{ mJ/m}^2$, which is the mean value of the MAE between [100] and [110] axis obtained from DFT, see Table I. In the DL region, there is an easy axis along the $\mathbf{e}_{u,DL}(\mathbf{r}) = [110]$ (out-of-plane) direction with a value of $K_{DL} = -4.58 \text{ mJ/m}^2$ of the ML.

SP-STM simulations. STM simulations have been performed in the spin-polarized generalization of the

Tersoff-Hamann model [42, 43]. The work function $\phi = 4.03 \text{ eV}$ of the Mn ML on Ta(110) was determined in DFT and leads to a vacuum decay of 10.3 nm^{-1} of the wave functions. A tip height of 0.6 nm was assumed.

REFERENCES

- * Email: felix.zahner@uni-hamburg.de; These two authors contributed equally to this work.
- † Email: drevelow@physik.uni-kiel.de; These two authors contributed equally to this work.
- [1] A. Fert, N. Reyren, and V. Cros, Magnetic skyrmions: advances in physics and potential applications, *Nature Reviews Materials* **2**, 17031 (2017).
- [2] R. Wiesendanger, Nanoscale magnetic skyrmions in metallic films and multilayers: a new twist for spintronics, *Nature Reviews Materials* **1**, 16044 (2016).
- [3] C. Back, V. Cros, H. Ebert, K. Everschor-Sitte, A. Fert, M. Garst, T. Ma, S. Mankovsky, T. L. Monchesky, M. Mostovoy, N. Nagaosa, S. S. P. Parkin, C. Pfleiderer, N. Reyren, A. Rosch, Y. Taguchi, Y. Tokura, K. von Bergmann, and J. Zang, The 2020 skyrmionics roadmap, *Journal of Physics D: Applied Physics* **53**, 363001 (2020).
- [4] N. Nagaosa and Y. Tokura, Topological properties and dynamics of magnetic skyrmions, *Nat. Nanotechnol.* **8**, 899 (2013).
- [5] B. Göbel, I. Mertig, and O. A. Tretiakov, Beyond skyrmions: Review and perspectives of alternative magnetic quasiparticles, *Physics Reports* **895**, 1 (2021), beyond skyrmions: Review and perspectives of alternative magnetic quasiparticles.
- [6] B. Göbel, A. Mook, J. Henk, I. Mertig, and O. A. Tretiakov, Magnetic bimerons as skyrmion analogues in in-plane magnets, *Phys. Rev. B* **99**, 060407 (2019).
- [7] R. Brüning, J. Bedow, R. Lo Conte, K. von Bergmann, D. K. Morr, and R. Wiesendanger, The Noncollinear Path to Two-Dimensional Topological Superconductivity, *ACS Nano* **19**, 36215 (2025).
- [8] N. Romming, C. Hanneken, M. Menzel, J. E. Bickel, B. Wolter, K. von Bergmann, A. Kubetzka, and R. Wiesendanger, Writing and deleting single magnetic skyrmions, *Science* **341**, 636 (2013).
- [9] C. Moreau-Luchaire, C. Moutafis, N. Reyren, J. Sampaio, C. A. F. Vaz, N. V. Horne, K. Bouzehouane, K. Garcia, C. Deranlot, P. Warincke, P. Wohlhüter, J.-M. George, M. Weigand, J. Raabe, V. Cros, and A. Fert, Additive interfacial chiral interaction in multilayers for stabilization of small individual skyrmions at room temperature, *Nat. Nanotechnol.* **11**, 444 (2016).
- [10] O. Boulle, J. Vogel, H. Yang, S. Pizzini, D. de Souza Chaves, A. Locatelli, T. O. Mentes, A. Sala, L. D. Buda-Prejbeanu, O. Klein, M. Belmeguenai, Y. Roussigné, A. Stashkevich, S. M. Chérif, L. Aballe, M. Foerster, M. Chshiev, S. Auffret, I. M. Miron, and G. Gaudin, Room-temperature chiral magnetic skyrmions in ultrathin magnetic nanostructures, *Nat. Nanotechnol.* **11**, 449 (2016).

- [11] S. Woo, K. Litzius, B. Krüger, M.-Y. Im, L. Caretta, K. Richter, M. Mann, A. Krone, R. M. Reeve, M. Weigand, P. Agrawal, I. Lemesh, M.-A. Mawass, P. Fischer, M. Kläui, and G. S. D. Beach, Observation of room-temperature magnetic skyrmions and their current-driven dynamics in ultrathin metallic ferromagnets, *Nat. Mater.* **15**, 501 (2016).
- [12] W. Jiang, X. Zhang, G. Yu, W. Zhang, X. Wang, M. B. Jungfleisch, J. E. Pearson, X. Cheng, O. Heinonen, K. L. Wang, Y. Zhou, A. Hoffmann, and S. G. E. te Velthuis, Direct observation of the skyrmion hall effect, *Nat. Phys.* **13**, 162 (2017).
- [13] K. Litzius, I. Lemesh, B. Krüger, P. Bassirian, L. Caretta, K. Richter, F. Büttner, K. Sato, O. A. Tretiakov, J. Förster, R. M. Reeve, M. Weigand, I. Bykova, H. Stoll, G. Schütz, G. S. D. Beach, and M. Kläui, Skyrmion Hall effect revealed by direct time-resolved X-ray microscopy, *Nat. Phys.* **13**, 170 (2017).
- [14] J. Spethmann, E. Y. Vedmedenko, R. Wiesendanger, A. Kubetzka, and K. von Bergmann, Zero-field skyrmionic states and in-field edge-skyrmions induced by boundary tuning, *Communications Physics* **5**, 19 (2022).
- [15] T. Jungwirth, X. Marti, P. Wadley, and J. Wunderlich, Antiferromagnetic spintronics, *Nature Nanotechnology* **11**, 231 (2016).
- [16] V. Baltz, A. Manchon, M. Tsoi, T. Moriyama, T. Ono, and Y. Tserkovnyak, Antiferromagnetic spintronics, *Rev. Mod. Phys.* **90**, 015005 (2018).
- [17] V. Bonbien, F. Zhuo, A. Salimath, O. Ly, A. Abbout, and A. Manchon, Topological aspects of antiferromagnets, *Journal of Physics D: Applied Physics* **55**, 103002 (2021).
- [18] J. Barker and O. A. Tretiakov, Static and dynamical properties of antiferromagnetic skyrmions in the presence of applied current and temperature, *Phys. Rev. Lett.* **116**, 147203 (2016).
- [19] X. Zhang, Y. Zhou, and M. Ezawa, Antiferromagnetic skyrmion: Stability, creation and manipulation, *Scientific Reports* **6**, 24795 (2016).
- [20] M. Bode, M. Heide, K. von Bergmann, P. Ferriani, S. Heinze, G. Bihlmayer, A. Kubetzka, O. Pietzsch, S. Blügel, and R. Wiesendanger, Chiral magnetic order at surfaces driven by inversion asymmetry, *Nature* **447**, 190 (2007).
- [21] B. Santos, J. M. Puerta, J. I. Cerdá, R. Stumpf, K. von Bergmann, R. Wiesendanger, M. Bode, K. F. McCarty, and J. de la Figuera, Structure and magnetism of ultrathin chromium layers on W(110), *New Journal of Physics* **10**, 013005 (2008).
- [22] B. Zimmermann, M. Heide, G. Bihlmayer, and S. Blügel, First-principles analysis of a homochiral cycloidal magnetic structure in a monolayer Cr on W(110), *Phys. Rev. B* **90**, 115427 (2014).
- [23] T. Dohi, S. DuttaGupta, S. Fukami, and H. Ohno, Formation and current-induced motion of synthetic antiferromagnetic skyrmion bubbles, *Nature Communications* **10**, 5153 (2019).
- [24] W. Legrand, D. Maccariello, F. Ajedas, S. Collin, A. Vecchiola, K. Bouzehouane, N. Reyren, V. Cros, and A. Fert, Room-temperature stabilization of antiferromagnetic skyrmions in synthetic antiferromagnets, *Nature Materials* **19**, 34 (2020).
- [25] H. Jani, J.-C. Lin, J. Chen, J. Harrison, F. Maccherozzi, J. Schad, S. Prakash, C.-B. Eom, A. Ariando, T. Venkatesan, and P. G. Radaelli, Antiferromagnetic half-skyrmions and bimerons at room temperature, *Nature* **590**, 74 (2021).
- [26] A. Aldarawsheh, I. L. Fernandes, S. Brinker, M. Sallermann, M. Abusaa, S. Blügel, and S. Lounis, Emergence of zero-field non-synthetic single and interchained antiferromagnetic skyrmions in thin films, *Nature Communications* **13**, 7369 (2022).
- [27] F. Zahner, F. Nickel, R. L. Conte, T. Drevelow, R. Wiesendanger, S. Heinze, and K. von Bergmann, Spin-polarized edge modes between different magnet-superconductor-hybrids (2025), arXiv:2506.16869 [cond-mat.supr-con].
- [28] S. Heinze, M. Bode, A. Kubetzka, O. Pietzsch, X. Nie, S. Blügel, and R. Wiesendanger, Real-space imaging of two-dimensional antiferromagnetism on the atomic scale, *Science* **288**, 1805 (2000).
- [29] R. Lo Conte, M. Bazarnik, K. Palotás, L. Rózsa, L. Szunyogh, A. Kubetzka, K. von Bergmann, and R. Wiesendanger, Coexistence of antiferromagnetism and superconductivity in Mn/Nb(110), *Physical Review B* **105**, L100406 (2022).
- [30] S. Meyer, M. Schmitt, M. Vogt, M. Bode, and S. Heinze, Dead magnetic layers at the interface: Moment quenching through hybridization and frustration, *Phys. Rev. Res.* **2**, 012075 (2020).
- [31] T. Eelbo, V. Zdravkov, and R. Wiesendanger, STM study of the preparation of clean Ta(110) and the subsequent growth of two-dimensional fe islands, *Surface Science* **653**, 113 (2016).
- [32] G. Kresse and J. Furthmüller, Efficient iterative schemes for ab initio total-energy calculations using a plane-wave basis set, *Phys. Rev. B* **54**, 11169 (1996).
- [33] G. Kresse and D. Joubert, From ultrasoft pseudopotentials to the projector augmented-wave method, *Phys. Rev. B* **59**, 1758 (1999).
- [34] J. P. Perdew and Y. Wang, Accurate and simple analytic representation of the electron-gas correlation energy, *Phys. Rev. B* **45**, 13244 (1992).
- [35] D. Wortmann, G. Michalicek, N. Baadji, M. Betsinger, G. Bihlmayer, J. Bröder, T. Burnus, J. Enkovaara, F. Freimuth, C. Friedrich, C.-R. Gerhorst, S. Granberg Cauchi, U. Grytsiuk, A. Hanke, J.-P. Hanke, M. Heide, S. Heinze, R. Hilgers, H. Janssen, D. A. Klüppelberg, R. Kovacik, P. Kurz, M. Lezaic, G. K. H. Madsen, Y. Mokrousov, A. Neukirchen, M. Redies, S. Rost, M. Schlipf, A. Schindlmayr, M. Winkelmann, and S. Blügel, *FLEUR*, Zenodo (2023).
- [36] S. H. Vosko, L. Wilk, and M. Nusair, Accurate spin-dependent electron liquid correlation energies for local spin density calculations: a critical analysis, *Canadian Journal of Physics* **58**, 1200 (1980).
- [37] P. Kurz, F. Förster, L. Nordström, G. Bihlmayer, and S. Blügel, Ab initio treatment of noncollinear magnets with the full-potential linearized augmented plane wave method, *Phys. Rev. B* **69**, 024415 (2004).
- [38] M. Heide, G. Bihlmayer, and S. Blügel, Describing Dzyaloshinskii–Moriya spirals from first principles, *Physica B Condens. Matter* **404**, 2678 (2009).
- [39] C. Li and A. J. Freeman and H. J. F. Jansen and C. L. Fu, Magnetic anisotropy in low-dimensional ferromagnetic systems: Fe monolayers on Ag(001), Au(001), and Pd(001) substrates, *Phys. Rev. B* **42**, 5433 (1990).
- [40] A. Vansteenkiste, J. Leliaert, M. Dvornik, M. Helsen,

- F. Garcia-Sanchez, and B. Van Waeyenberge, The design and verification of mumax3, *AIP Advances* **4**, 107133 (2014).
- [41] J. Mulkers, B. Van Waeyenberge, and M. V. Milošević, Effects of spatially engineered Dzyaloshinskii-Moriya interaction in ferromagnetic films, *Phys. Rev. B* **95**, 144401 (2017).
- [42] D. Wortmann, S. Heinze, P. Kurz, G. Bihlmayer, and S. Blügel, Resolving complex atomic-scale spin structures by spin-polarized scanning tunneling microscopy, *Phys. Rev. Lett.* **86**, 4132 (2001).
- [43] S. Heinze, Simulation of spin-polarized scanning tunneling microscopy images of nanoscale non-collinear magnetic structures, *Appl. Phys. A* **85**, 407 (2006).
- [44] See <https://www.nhr-verein.de/unsere-partner>.

ACKNOWLEDGEMENT

K.v.B. acknowledges financial support from the Deutsche Forschungsgemeinschaft (DFG, German Research Foundation) via project no. 402843438. S.H.

thanks the DFG for funding via project no. 462602351. The authors gratefully acknowledge the computing time made available to them on the high-performance computers “Lise” at the NHR center NHR@ZIB and “Emmy” at the NHR center NHR@Göttingen. This center is jointly supported by the Federal Ministry of Education and Research and the state governments participating in the NHR [44].

AUTHOR CONTRIBUTIONS

F.Z. and R.L.C. prepared the samples. F.Z. performed the experiments and together with R.L.C. and K.v.B. analyzed and discussed the data. T.D. performed the DFT calculations, developed the micromagnetic model, and analyzed the theoretical data together with S.H.. F.Z., T.D., S.H., and K.v.B. wrote the manuscript with contributions from all authors.